Modeling Gas Adsorption−Desorption Hysteresis in Energetically Heterogeneous Coal and Shale

Min Chen,* Shakil A. Masum, Sivachidambaram Sadasivam, Hywel R. Thomas, and Andrew C. Mitchell
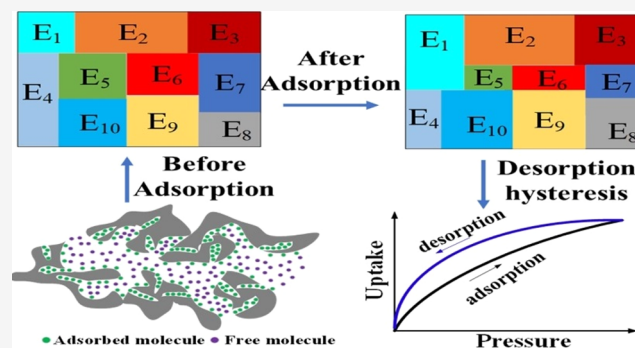
Read Online

ACCESS | Metrics & More | Article Recommendations

ABSTRACT: Adsorption of gases in porous adsorbents such as coal and shale generally exhibits the phenomenon of hysteresis. Most of the previous studies on desorption hysteresis were conducted via experimental tests. However, few theoretical models that represent adsorption−desorption hysteresis of gases in porous sorbents are available. To address this issue, this work develops a new adsorption−desorption model for describing adsorption and desorption isotherms of gases with hysteresis. Particularly, the energetically heterogeneous surfaces of an adsorbent are considered via the patchwise model. Based on the change in site energy distribution, a logarithmically pressure-dependent hysteresis index, which is used to measure the degree of hysteresis, is derived for quantitative assessment of the degree of hysteresis. Besides, the correlation between the desorption isotherm and initialized pressure for desorption is established. The accuracy of the proposed model to adequately describe the adsorption−desorption hysteresis of gas in coal and shale is demonstrated by validating the model against laboratory experiments obtained from the literature. The results indicate that the adsorption isotherm depends significantly on site energy distribution. By comparing the site energy distributions for adsorption and desorption isotherms, it is found that the desorption hysteresis can be attributed to the change in pore size distribution caused by adsorption-induced deformation. The analyses support that the proposed model can be used as an effective tool to quantitatively predict the amount of released gas during desorption, which is significant for designing coalbed methane or shale gas production and assessing long-term CO_2 storage behavior.

1. INTRODUCTION

It is well-known that gas adsorption in the internal pores of rock matrices is one of the important gas storage mechanisms in coal or shale reservoirs, and the adsorption capacity influences the gas content of these reservoirs.[1,2] The amount of adsorbed gas in coal or shale can be influenced by several controlling factors, such as coal type, pressure, temperature, and moisture content.[3−8] However, gas adsorption, generally, is not a fully reversible process. Experimentally measured adsorption isotherms do not coincide with corresponding desorption isotherms determined over the same pressure range on the same samples. This phenomenon, known as adsorption−desorption hysteresis, has been observed in many experimental studies.[9−13]

Desorption occurs during the recovery of coalbed methane (CBM) or shale gas when a depressurization technique is adopted for reservoir production. Bell and Rakop[14] reported that the nonlinearity in the desorption isotherm was more than that of the adsorption isotherm, and the pressure in the reservoirs is required to drop below the adsorption pressures to release the same amount of methane and achieve a good performance. The study by Ekundayo and Rezaee[15] revealed

that only using the adsorption isotherm, that is, ignoring the desorption hysteresis, overestimated the true contribution of gas desorption to shale gas production. In the case of carbon dioxide (CO_2) sequestration in coal, CO_2 desorption may become important after the gas injection operation is ceased. Higher CO_2 pressure that prevails in the vicinity of an injection well (during the injection stage) is expected to diminish until it reaches a steady state with respect to the pressure across the reservoir. The relaxation of pressure can drive a portion of the weakly sorbed CO_2 gas molecules to desorb into the free gas phase, and such a phenomenon was observed by Sadasivam et al.[13] in their laboratory-based (manometric) sorption studies involving intact bituminous coal samples. Wang et al. also emphasized on the role of desorption hysteresis in assessing

long-term containment and stability of stored CO_2 in coal deposits. If the degree of hysteresis is significant, more injected gas will adsorb in coal reservoirs. This means that desorption isotherm and adsorption−desorption hysteresis should be considered for carrying out the long-term CO_2 storage assessment, and therefore, it has been identified as one of objectives of this work.

The explanation of desorption hysteresis in porous materials is contentious. Both capillary condensation and pore blocking are used to explain hysteresis.[16−20] According to the former concept, the formation of a meniscus near the pore mouths and its movement toward the pore interior during desorption lead to the deviation of the desorption isotherm from the adsorption isotherm.[18,19] The pore blocking model assumes an ink bottle pore structure. Due to such a structure, for a pore to become empty, the adjacent connected pores need to be emptied first as vapor evaporating from a pore requires preferential pathways to be available. This therefore drives the hysteresis.[18,20] However, attributing gas adsorption hysteresis to coal and shale for capillary condensation seems improbable because coal and shale contain a large number of micropores (<2 nm),[21,22] where capillary condensation cannot happen. Hysteresis is also observed for low-critical-temperature gases, such as methane (CH_4), but such gases cannot experience condensation at general reservoir conditions.[19,23] This suggests that the capillary effect is unbale to explain gas adsorption−desorption hysteresis in coal and shale formations.[9,23,24] The experimental study by Chen et al.[25] indicates that the pore structure of undeformed coal is controlled by mesopores with a narrow, slit-shaped morphology and good interconnectivity; therefore, pore blocking is insufficient for the explanation of the hysteresis phenomenon. Goodman et al.[26] attributed the adsorption hysteresis to residual moisture contents of the coal samples. However, desorption hysteresis was observed during adsorption experiments conducted on dry coals by Hou et al.[10]

Quantitative evaluation of the hysteresis degree is also necessary since the hysteresis loop, formed by adsorption and desorption isotherms, varies significantly across different adsorption systems. Many studies evaluated the hysteresis degree qualitatively, that is, by using the terminologies such as "no", "weak", and "significant".[9] Several empirical indices for quantifying the hysteresis degree or irreversibility between adsorption and desorption isotherms for soil, polymers, organic matter, and other porous materials can be found in the study by Sander et al.[27] Among these, the areal hysteresis index (AHI) method is widely used for quantifying adsorption−desorption hysteresis of gas−coal or gas−shale systems. The AHI is defined as the area covered by a hysteresis loop, formed between the areas bounded by the desorption isotherm and the adsorption isotherm.[10,28] For different initial pressures, the parameters of a desorption isotherm that takes the form of a Langmuir isotherm are different, and consequently, the AHI should be re-estimated. Thus, the AHI is only applicable to single-step desorption isotherms, which are not applicable to practical/field conditions where the initial pressure, at which desorption may occur, often varies with locations. One of the primary objectives is to present an index to measure the hysteresis degree.

2. BACKGROUND OF MODEL DEVELOPMENT

Gas storage by physical adsorption occurs in the coal matrices and shale formations, for example,[29,30] and the sorption hysteresis phenomenon has been observed extensively.[9,12,13,31] Although the hysteresis phenomenon is evident in adsorbent−
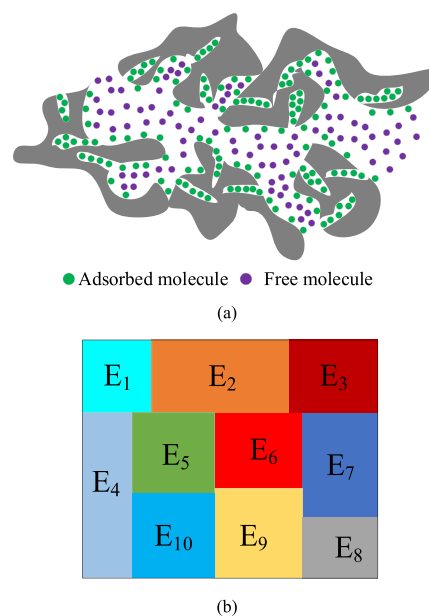

● Adsorbed molecule   ● Free molecule

(a)

(b)

Figure 1. (a) Schematic illustration of gas adsorption in heterogeneous porous media where different size pores contain different adsorption sites and (b) concept of surface topography composed of finite homogeneous patches, where each of these patches contains adsorption sites with the same binding energy.

adsorbate systems, there is still no consensus on the origin of desorption hysteresis. In addition to the mechanisms mentioned above, pore deformation was also used to explain the occurrence of adsorption hysteresis, which has precedence in explaining the hysteresis behavior of gases on glassy synthetic polymers.[27,32] This explanation has recently been verified by Chen et al.[33] Through molecular simulations, it was found that the polymer swells to form water−polymer hydrogen bonds upon adsorption, while these hydrogen bonds do not break upon desorption at the same vapor pressure. In comparison, pore deformation also seems to be a reasonable explanation for the origin of adsorption hysteresis in porous geomaterials such as coal and shale. The study by Alafnan[23] indicated that adsorption causes internal structural changes and swelling in the organic matter of shale, leading to an alteration of the pore space available for molecule retention during adsorption and desorption paths and eventually to hysteresis. Similar explanations were also reported by McCutcheon et al.[34] and Wang et al.[9] Although pore deformation has been considered as an explanation for the hysteresis phenomenon, the underlying mechanism for how pore deformation leads to hysteresis occurrence is still unclear.

As mentioned above, except for some empirical indices for evaluating adsorption hysteresis, few theoretical models are available in the literature that represent the desorption process, especially under different initial pressures, although desorption isotherm varies with different initial pressure where desorption begins.[30] In addition, most of studies assume that the solid surface is homogeneous and adopted the Langmuir isotherm to capture the gas adsorption behavior in coal and shale. Nevertheless, pore surfaces of the adsorbent contain various adsorption sites for affixing adsorbate molecules, as shown in Figure 1a. The surface heterogeneity should be accounted for.

The objectives of this work are (1) to develop an adsorption−desorption model for hysteretic desorption of gases in energetically heterogeneous geomaterials such as coal and

shale; (2) to account for the impact of initial pressure where desorption begins on desorption hysteresis; (3) to derive a measure of hysteresis (hysteresis index, HI) for quantitative assessment of the hysteresis degree; and (4) to reveal the underlying mechanism for pore deformation-induced desorption hysteresis using the developed model. As shown in Figure 1a, the interaction energy between the adsorbate and the adsorbent varies with different types of adsorption sites;[35] in this study, the energetically heterogeneous surface of an adsorbent is characterized by the patchwise or homotattic model, which is used to conceptualize the complex adsorption sites topography, and adsorption sites of the same interaction energy are contained in a single patch (different colors denote different interaction energies of patches, E1, E2, E3...), as shown in Figure 1b. The size of each homogeneous patch is defined using the adsorption site energy distribution (ASED) function. The HI is derived based on the difference in site energy distribution between adsorption and desorption isotherms. By incorporating the HI into the adsorption isotherm, the desorption isotherm model is obtained. Particularly, a correlation between the desorption isotherm and initial pressure where desorption begins is obtained. The reliability of the developed adsorption–desorption model has been evaluated by validating against experimental data on adsorption/desorption of various gases in coal and shale. The sensitivity analysis of the model parameters is performed, and the variation of site energy distribution due to gas adsorption is discussed. The cause of adsorption–desorption hysteresis is revealed through considering the change in site energy distribution between adsorption and desorption processes. Finally, an application example of the model to investigate the long-term fate of sequestered CO_2 in a coal seam is presented to demonstrate the applicability of the developed model.

3. ADSORPTION–DESORPTION MODEL FOR A HETEROGENEOUS SOLID SURFACE

It is assumed that only one molecule can be adsorbed on one adsorption site, and the total fractional surface coverage θ_t can be
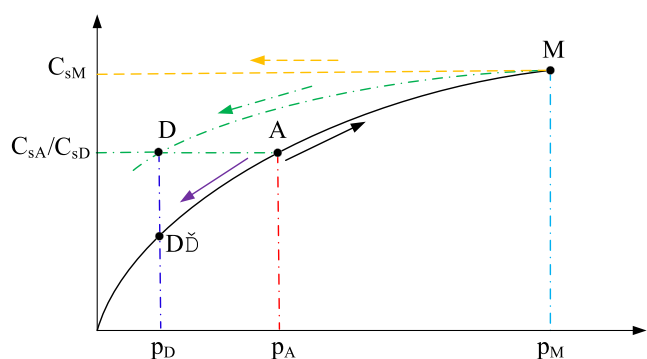

Figure 2. Schematic representation of different adsorption and desorption states for the calculation of the HI.

defined as the total number of adsorbed molecules and available sites

$$\theta_t = \frac{C_s}{C_L} \tag{1}$$

where C_s is the total amount of the adsorbed molecules and C_L is the maximum adsorbed amount of the sorbent.

The total adsorbed sites, C_s, is the sum of the adsorption sites occupied by molecules at all of the available patches

$$C_s = \sum_{i=1}^{N} C_{si} \tag{2}$$

where N is the number of types of available adsorption sites or patches and C_{si} is the amount of adsorbed gas at the ith patch.

Also, the maximum adsorbed amount (C_L) of the sorbents is reached when all adsorption sites are occupied by molecules. This is expressed as a sum of the local adsorption sites of each patch, that is

$$C_L = \sum_{i=1}^{N} C_{Li} \tag{3}$$

where C_{Li} is the local adsorption capacity at the ith patch.

Equation 1 can be re-arranged using eqs 2 and 3, expressed as

$$\theta_t = \frac{\sum_{i=1}^{N} C_{si}}{C_L} = \sum_{i=1}^{N} \frac{C_{Li}}{C_L} \frac{C_{si}}{C_{Li}} = \sum_{i=1}^{N} F_i(E_i)\theta_i(E_i) \tag{4}$$

where $F_i(E_i) = \frac{C_{Li}}{C_L}$, $\theta_i(E_i) = \frac{C_{si}}{C_{Li}}$, the former representing the fraction of local available adsorption sites to total available adsorption sites and the latter representing the local adsorption uptake in different types of adsorption sites, and E_i is the interaction energy between the adsorbate and the adsorbent. Assuming that $F(E)$ is a continuous function, mathematically, the total coverage of a heterogeneous surface with quasi-static energy sites, θ_t, can be expressed in the integration form

$$\theta_t = \int_0^\infty \theta(E)F(E) \, dE \tag{5}$$

where $F \, dE$ is the fraction of the surface with adsorption energy between E and $E + dE$. From eq 3, $F(E)$ fulfills the following normalization condition

$$\int_0^\infty F(E) \, dE = 1 \tag{6}$$

From eq 5, the total fractional occupancy of all adsorption sites, θ_t, can be calculated when the local fractional occupancy of the adsorption site $\theta(E)$ and the energy distribution function $F(E)$ are known. As shown in Figure 1, gas adsorption onto the solid surface is a kinetic process. As each patch is considered to be a homogeneous surface, this process can be described by the classical absolute rate theory,[36,37] given as

$$\frac{d\theta_i}{dt} = k_{ai}p(1 - \theta_i) - k_{di}\theta_i \tag{7}$$

$$k_{ai} = k_a \exp\left(-\frac{E_{ai}}{RT}\right) \quad \text{and} \quad k_{di} = k_d \exp\left(-\frac{E_{di}}{RT}\right) \tag{8}$$

where E_{ai} and E_{di} are the activation energies for adsorption and desorption, respectively, k_a and k_d are the rate constant for adsorption and desorption, respectively, p is the pressure, T is the temperature, and R is the universal gas constant. The first term on the right-hand side of eq 7 represents the rate of adsorption and the second term represents the desorption rate.

When gas sorption reaches equilibrium, $\frac{d\theta_i}{dt} = 0$, eq 7 is reduced to

$$\theta_i = \frac{Kp \exp\left(\frac{E_i}{RT}\right)}{1 + Kp \exp\left(\frac{E_i}{RT}\right)} \tag{9}$$

where $K = \frac{k_a}{k_d}$ and $E_i = E_{di} - E_{ai}$.

Since $E_c = -RT \ln(Kp)$,[38] eq 9 above becomes

$$\theta_i = \frac{\exp\left(\frac{E_i - E_c}{RT}\right)}{1 + \exp\left(\frac{E_i - E_c}{RT}\right)} \tag{10}$$

By application of the condensation approximation to eq 10, θ_i can be expressed as a Heaviside step function[39,40]

$$\theta_i = \begin{cases} 0 & E_i < E_c \\ 1 & E_i \geq E_c \end{cases} \tag{11}$$

where E_c is the critical energy level of the adsorbate molecule,[39] and it determines which adsorption sites can be occupied by adsorbate molecules.

Therefore, eq 5 can be rewritten as

$$\theta_t = \int_0^{E_c} 0 \, dE + \int_{E_c}^{\infty} F(E) \, dE = \int_{E_c}^{\infty} F(E) \, dE \tag{12}$$

For the patchwise topography, $F(E)$ is known as the adsorption energy distribution function. From eq 9, it can be seen that the total adsorption uptake only depends on the distribution function of adsorption energy sites. In this study, quasi-Gaussian adsorption energy distribution, which has been successfully applied to theoretical descriptions of adsorption on energetically heterogeneous solid surfaces in the literature, is used to capture the characteristics of the energy distribution of adsorption sites[41,42]

$$F(E) = \frac{1}{c} \frac{\exp\left(\frac{E - E_0}{c}\right)}{\left[1 + \exp\left(\frac{E - E_0}{c}\right)\right]^2} \tag{13}$$

where E_0 is the mathematical expectation, representing the adsorption energy site with a maximum fraction. c is the standard deviation from the mean value of the energy distribution curve. It is a measure of the degree of surface energetic heterogeneity in a physical sense.

Substituting eqs 13 into 12 and integrating over the available adsorption energy site yield the total adsorption uptake

$$\theta_t = \frac{1}{1 + \exp\left(\frac{E_c - E_0}{c}\right)} \tag{14}$$

Inserting $E_c = -RT \ln(Kp)$ into eq 14, it becomes

$$\theta_t = \frac{\left[Kp \exp\left(\frac{E_0}{RT}\right)\right]^{RT/c}}{1 + \left[Kp \exp\left(\frac{E_0}{RT}\right)\right]^{RT/c}} \tag{15}$$

Under isothermal conditions, using the definitions $K \exp\left(\frac{E_0}{RT}\right) = K_{LF}$ and $RT/c = n$, eq 14 takes the form of the commonly used Langmuir−Freundlich isotherm

$$\theta_t = \frac{(pK_{LF})^n}{1 + (pK_{LF})^n} \tag{16}$$

$$C_s = C_L \theta_t = \frac{C_L(pK_{LF})^n}{1 + (pK_{LF})^n} \tag{17}$$

When n equals 1 in eqs 16 and 17, the Langmuir−Freundlich isotherm is reduced to the Langmuir isotherm. Equations 1−17 present the derivation of an adsorption isotherm based on the adsorption energy distribution function. Subsequently, the correlation between the adsorption isotherm and the desorption isotherm will be elaborated.

Before presenting the desorption isotherm, the HI, which is used to quantify the degree of hysteresis, will be derived here. Due to adsorption−desorption hysteresis, the desorption curve generally does not coincide with adsorption curve, and the dependence of the desorption curve on the adsorption state from which desorption is initiated is observed as well. Also, to establish the desorption isotherm, boundary conditions have to be satisfied: (1) at the state where depressurization begins, the desorption curve and adsorption curve are intersected, that is, the adsorbed amounts estimated from both the curves are the same, as shown by state M ($p = p_M$ and $C_s = C_{sM}$) in Figure 2; (2) when pressure decreases to zero, all the adsorbed amount (physisorption) is reduced to zero as well; (3) when the sorption is fully irreversible (chemisorption), the adsorbed amount remains at the value reached before desorption initiation, as indicated by the yellow arrow of Figure 2; and (4) if the sorption is fully reversible, the desorption isotherm (purple arrow in Figure 2) should be reduced to the adsorption isotherm (black arrow in Figure 2).

Considering another two different states D and A, as shown in Figure 2: state D ($p = p_D$, $C_s = C_{sD}$) is the generally measured desorption state, which deviates from its expected position on the sorption curve (state D′ having the same critical energy level as that of state D) due to the desorption hysteresis and state A ($p = p_A$, $C_s = C_{sA}$) is the fully reversible desorption state where there are the same adsorbed molecules as those in state D. The change in the adsorption energy level from state A to state D is

$$\Delta E_{cAD} = E_{cA} - E_{cD} \tag{18}$$

The difference in the energy level between states M and D is then

$$\Delta E_{cMD} = E_{cM} - E_{cD} \tag{19}$$

The ratio of ΔE_{cAD} to ΔE_{cMD} is defined as an index to evaluate the degree of adsorption hysteresis

$$HI = \frac{\Delta E_{cAD}}{\Delta E_{cMD}} = \frac{\ln p_D - \ln p_A}{\ln p_D - \ln p_M} \tag{20}$$

Sander et al.[27] derived a similar index, the thermodynamic index of irreversibility (TII) based on the difference in the chemical potential between states for quantifying the adsorption hysteresis. From eq 20, it can be seen that the degree of hysteresis is logarithmically dependent on gas pressure.

After rearrangement, eq 20 becomes

$$p_A = p_D^{1-HI} p_M^{HI} \tag{21}$$

Substituting eqs 21 into 17 and replacing p_D with p, the desorption isotherm is taken in the following form

$$C_s = \frac{C_L(K_{LF} p_M^{HI} p^{1-HI})^n}{1 + (K_{LF} p_M^{HI} p^{1-HI})^n} \tag{22}$$

Equation 22 still takes the form of the Langmuir–Freundlich isotherm. It can be seen from eq 22 that the desorption curve depends on the initial pressure where depressurization begins. Equation 22 is able to satisfy the conditions mentioned above. When p equals to p_M, the adsorbed amount predicted by the adsorption isotherm and the desorption isotherm, C_s, are identical. Pressure drops to zero, $C_s = 0$. Adsorption hysteresis can be observed when the index HI falls in between 0 and 1. A completely reversible adsorption process can be achieved when the index HI is 0. The adsorption process is fully irreversibility (chemisorption) if the index HI approaches 1. These two extreme conditions indicate that the index HI ranges from 0 to 1, and this will be checked in following section for exercises.

4. MODEL VALIDATION

In this section, the proposed model is evaluated against published experimental data on adsorption/desorption behavior
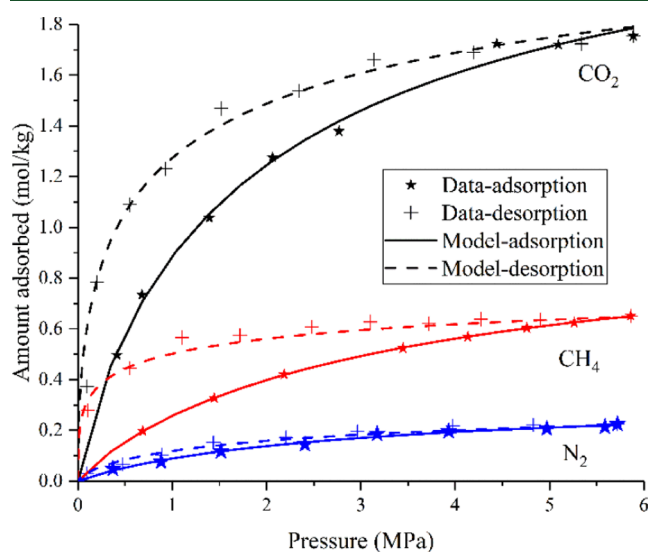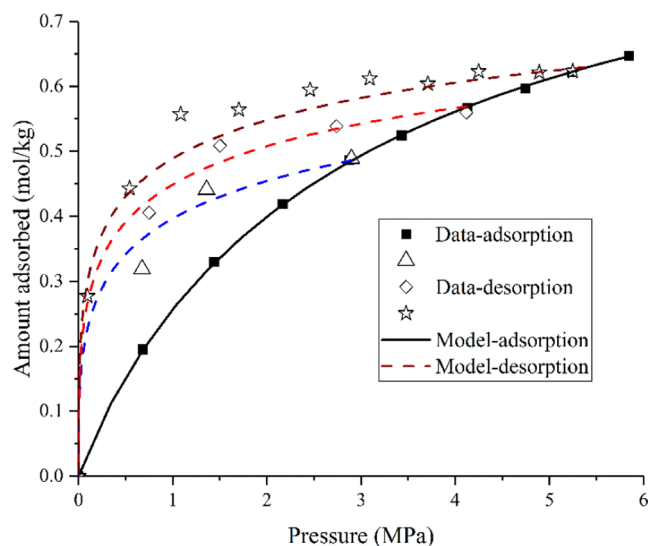
Figure 4. Comparison of results predicted by the model with the experimental data by Jessen et al.[43] on desorption of CH_4 at different initial pressures where depressurization begins (△, ◇, and ☆ are desorption isotherms for depressurizations beginning at 5.52, 4.14, and 2.76 MPa, respectively).

Figure 3. Comparison of results predicted by the model with experimental data of CO_2, CH_4, and N_2 adsorption/desorption on Power River Basin (Wyoming) coal samples.[43]

Table 1. Parameters Obtained from Fitting the Data of Jessen et al.[43]

parameters	adsorption capacity C_L (mol/kg)	constant, K_{LF}, (MPa^{-1})	exponent, n, (−)	index, HI or TII, (−)
CO_2	2.49	0.496	0.861	0.42
CH_4	1.00	0.328	0.951	0.64
N_2	0.35	0.322	0.932	0.25

in coals and shales. Jessen et al.[43] measured the equilibrium adsorption properties of CH_4, CO_2, and N_2 in coal samples from the Powder River Basin, Wyoming. All adsorption–desorption measurements were conducted at 295.15 K using a gravimetric method. To investigate the CH_4 coal adsorption hysteresis, He et al.[44] tested the CH_4 adsorption–desorption behavior of six coal samples (P8, P5, QN, TY, HSW, and JH) obtained from three main coal fields in China. The CH_4 coal sorption measurement was performed at 308.15 K and pressures up to 5.5 MPa using a high-pressure volumetric analysis system. Zhao et al.[31] measured adsorption/desorption of CO_2 and various light hydrocarbons including CH_4, ethane (C_2H_6), propane (C_3H_8), n-butane (n-C_4H_{10}), and iso-butane (iso-C_4H_{10}) in two different

shale samples. One shale sample (Kimmeridge Blackstone) is from the Blackstone band of the Kimmeridge Clay Formation from an outcrop east of Kimmeridge Bay in Dorset, UK. The other (Neuquén Shale) is from a Neuquén Basin well, Argentina. The sorption measurements of two shales were performed at three different temperatures of 308.15, 323.15, and 338.15 K. In this work, the experimental results at 308.15 K were collected to validate the proposed model. Parameters obtained from the experimental data fit for coals are listed in Tables 1 and 2. The comparisons between experimental measurements on coals and model predictions are shown in Figures 3−5. Table A1 in Appendix A lists the parameters used for matching experimental data from Zhao et al.[31] Figures A1 and A2 in Appendix A present the comparison of results between the model and experimental measurements.

The results of fitting the experimental data reported by Jessen et al.[43] on adsorption and desorption versus pressure for pure CO_2, CH_4, and N_2 using the constructed model, that is, eqs 14 and 19, are shown in Figure 3. Gas is mainly physically adsorbed in coal,[30] and the adsorbed gas can be released after the pressure drop. The good agreement between model predictions and experimental data demonstrates the reliability of the model to study adsorption–desorption equilibrium behavior. At around the same pressure range, CO_2 adsorption is substantially larger than that of CH_4 and N_2. N_2 has the lowest adsorption capacity among these gases. The variation in adsorption isotherms for CO_2, CH_4, and N_2 indicates that although the adsorbent is the same, the site energy distribution function differs with adsorbates, as detailed in the next section.

During the desorption tests all gases displayed hysteresis. The least amount of hysteresis was observed for N_2. This can also be revealed by the fact that the value of the HI for N_2, listed in Table 1, is the lowest compared to those for CO_2 and CH_4. Although CO_2 shows the highest adsorption capacity for the given coal sample, its TII (=0.42) is lower than that of CH_4 (0.64). This indicates that the degree of desorption hysteresis for CH_4 is stronger than that for CO_2, and pressure should drop to a lower pressure for CH_4 desorption. Similar finding was also reported
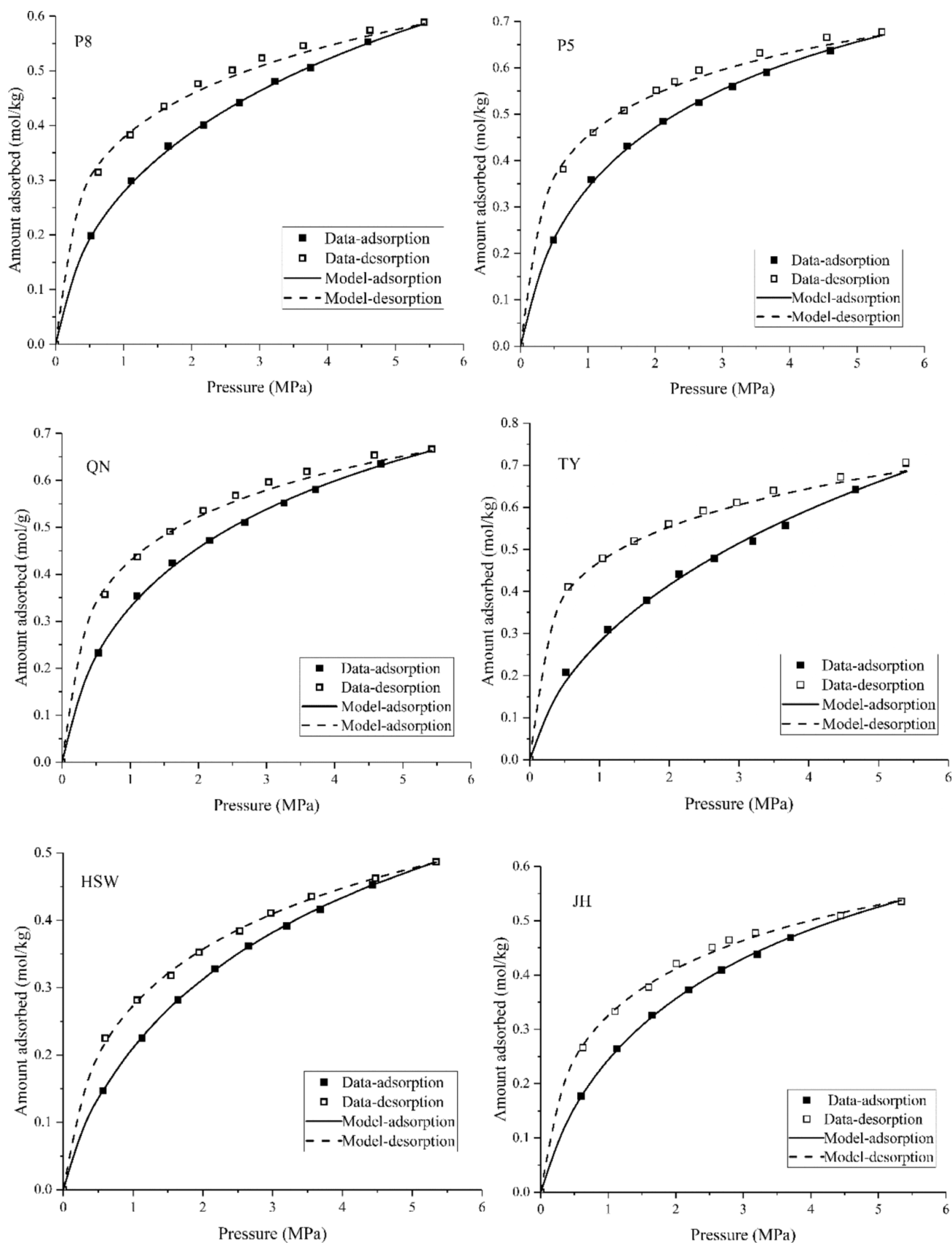
Figure 5. Comparison of results predicted by the model with the experimental data of He et al.[44] on CH_4 adsorption−desorption on coals.

by Zhou et al.[30] This may be because the change in pore size distribution caused by CO_2 adsorption is different from that by CH_4. A number of experimental studies have observed that the CO_2 adsorption-induced swelling is much larger than that of

Table 2. Parameters Obtained from Fitting the Data of He et al.[44]

samples	adsorption capacity C_L (mol/kg)	constant, K_{LF}, (MPa^{-1})	exponent, n, (−)	index, HI or TII, (−)
P8	1.55	0.081	0.602	0.38
P5	1.13	0.315	0.717	0.36
QN	1.26	0.218	0.673	0.33
TY	2.18	0.057	0.658	0.54
HSW	0.91	0.221	0.797	0.27
JH	0.94	0.273	0.798	0.31

CH_4.[45] CO_2 adsorption-induced pore deformation could lead to a greater increase in larger size pores, in contrast to CH_4 adsorption with a greater increase in smaller size pores.

Jessen et al.[43] measured CH_4 desorption at different initial pressures where desorption began, as shown in Figure 4. It shows that CH_4 desorption follows different paths as the gas pressure reduction for desorption begins at 5.52, 4.14, and 2.76 MPa. This implies that the desorption process followed during pressure drops is influenced by the initial maximum pressure, and the site energy distribution can be influenced by the gas adsorption process. The fitting results of model is illustrated in Figure 4, and the parameters listed in Table 1 for CH_4 are used for fitting. A good agreement between the model predictions and experimental results is achieved, although a slight deviation is observed for mediate pressure (1.0–3.0 MPa) when the initial pressure for desorption is higher. The deviation is perhaps due to (1) the experimental error, for example, desorption time is not sufficient for complete desorption, as indicated by fluctuant experimental desorption data; in a physical sense, the adsorption amount for lower pressure should not be larger than that for higher pressure; or (2) the assumption of a constant HI. In this work, the HI is considered to be constant regardless of where the desorption on the adsorption curve initiates. The relationship between the HI and pressure or adsorbed amount is neglected. A recent study by Borisover[46] suggested that the calculation of the HI should take the adsorption amount into account. More

experimental tests on desorption at different initial pressures are required to comprehensively understand such a correlation.

Figure 5 shows the results of fitting experimental data tested by He et al.[44] on the six coal samples. Table 2 lists the fitting parameters. The exponent n and HI, for all samples fall within the range between 0 and 1. Excellent agreements between the model predictions and the benchmark data indicate that the proposed model can adequately predict the adsorption–desorption isotherms using the patchwise ASED concept.

5. RESULTS AND DISCUSSION

The ASED is considered for the derivation of the adsorption/desorption isotherm. Since the ASED correlates the adsorption isotherm parameters with the energetic heterogeneity of the adsorbent surface, theoretical insights into the ASED from the isotherm equation will be extracted using the isotherm parameters.

5.1. Characteristics of Sorption Site Energy Distribution. In this study, the ASED is approximated by a quasi-Gaussian distribution. As mentioned in section 2, the mean site energy E_0 and standard deviation c control the site energy distribution. Under isotherm conditions, the isotherm constants K_{LF} and n are able to reflect the site energy E_0 and standard deviation c. Figure 6 shows the effect of a change in the isotherm constant n on the adsorption isotherm or the standard deviation c on the ASED. Varying the value of n means different surface heterogeneities and the same energy strength. The ASED spectra and their corresponding adsorption isotherms are constructed using the above eqs 13–15 with some assumed values for the isotherm constants. Figure 6a shows that the larger the value of n, the narrower the site energy distribution, and the higher the frequency of mean energy. When the value of n is lower, high energy adsorption sites displays higher probability. A rapid increase in the surface coverage occurs at low pressure, while the increase in uptake is slow at high pressure due to the lower probability of low energy adsorption sites (Figure 6b). On the contrary, the contribution of sites with lower binding energy
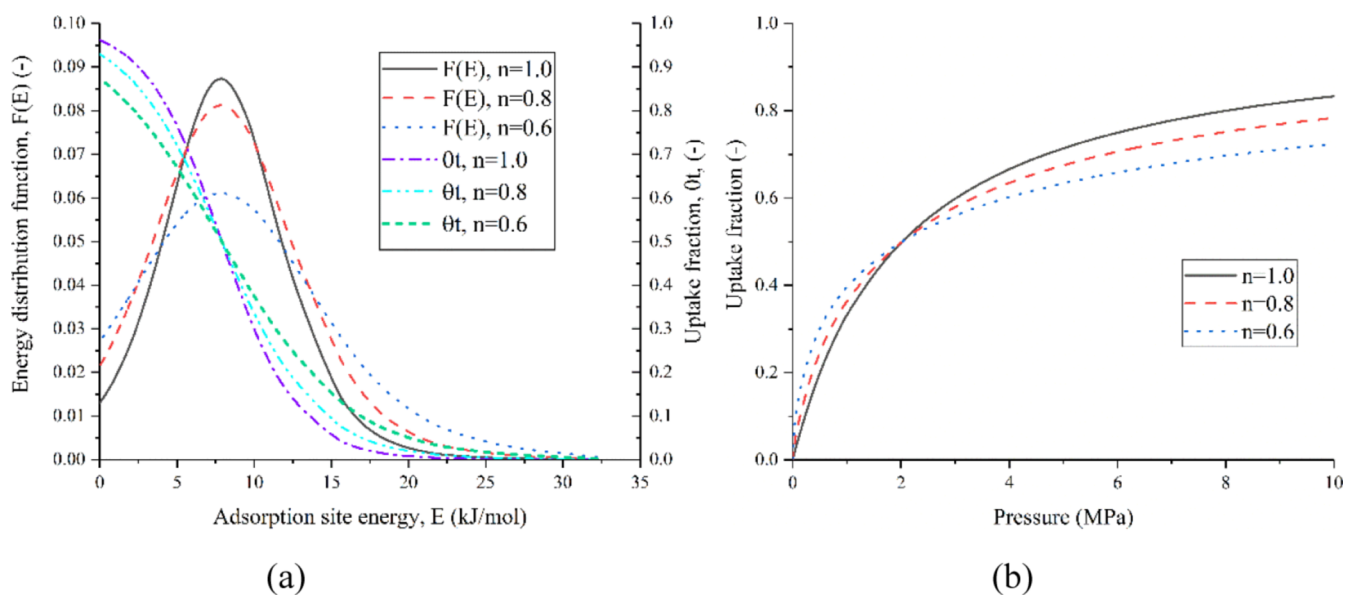

Figure 6. (a) Site energy distribution function, $F(E)$, and cumulative uptake, $\theta_t(E)$, according to the adsorption isotherm for different values of $n = 1.0$, 0.8, and 0.6 and (b) corresponding adsorption isotherm (given that $T = 295$ K, $K_{LF} = 0.5$ MPa^{-1} or $E_0 = 7.9$ kJ/mol, and $n = 0.6$, 0.8, and 1.0 or $c = 2.45$, 3.07, and 4.09 kJ/mol).
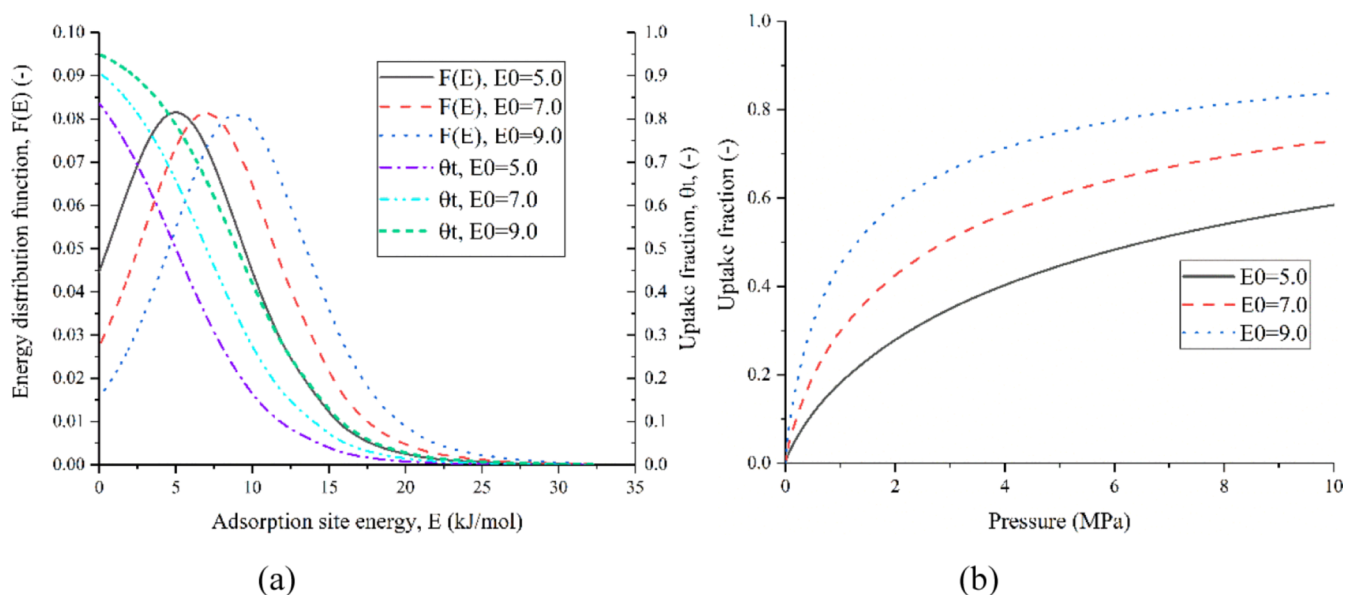
Figure 7. (a) Site energy distribution function, $F(E)$, and cumulative uptake, θ_v, for different values of $E_0 = 5.0$, 7.0, and 9.0 kJ and (b) adsorption isotherms for different values of E_0 (given that $T = 295$ K, $E_0 = 5.0$, 7.0, and 9.0 kJ/mol or $K_{LF} = 0.15$, 0.35, and 0.78 MPa^{-1}, and $n = 0.8$ or $c = 3.07$ kJ/mol).
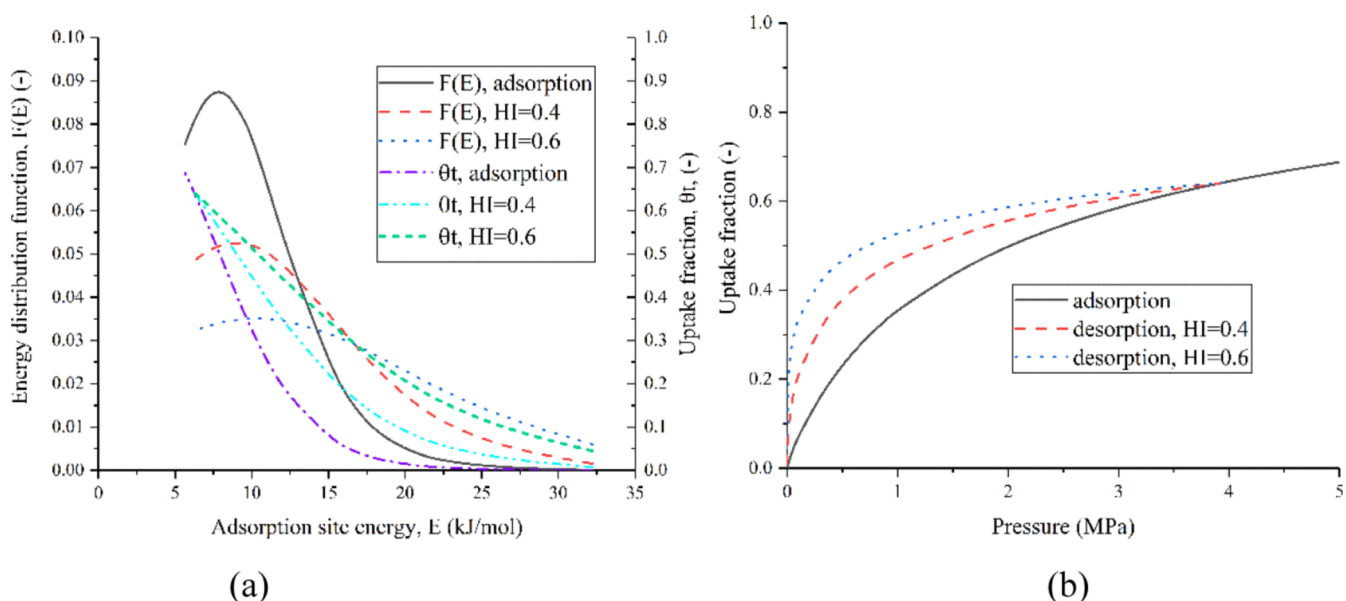

Figure 8. (a) Site energy distribution function, $F(E)$, and cumulative uptake, θ_v, for different degrees of adsorption hysteresis and (b) desorption isotherms for different degrees of adsorption hysteresis (given that $T = 295$ K, $p_M = 4$ MPa, $K_{LF} = 0.5$ MPa^{-1}, $n = 0.86$, and HI = 0.4 and 0.6).

to gas adsorption is larger as pressure increases when the value of n is larger.

Figure 7 illustrates the effect of change in the isotherm constant K_{LF} on the adsorption isotherm or mean energy E_0 on the ASED. Varying the value of K_{LF} or E_0 represents the same surface heterogeneity and different energy strengths. The values of constants are provided in the caption of the figure. Figure 7 shows that the effect of binding energy strengths on gas adsorption is more significant. When mean energy is higher, the contribution of high energy sites to gas adsorption is significantly larger than that of the low energy sites at the low pressure condition, and this is because high energy adsorption sites have a higher probability when mean energy is higher. In comparison, the contribution of a site with low binding energy to gas uptake is

more significant at the high pressure condition when mean energy is lower. For lower values of E_0 and n, an exponential distribution of site energies at lower pressures is observed. A negative correlation between pore size and adsorption energy has been reported in studies by Stoeckli et al.,[47] Burhan et al.,[39] and Li et al.[48] The greater the mean site energy, the smaller the size of pores. In larger pores of a sorbent, the mean site energy will be lower. Figure 7 shows that the higher mean site energy results in a more rapid increase in surface coverage at low pressure conditions. This suggests that the gas adsorption in porous sorbents occurs first in micropores at low pressure conditions.

5.2. Change in Site Energy Distribution. The desorption isotherm (eq 22) can be rewritten in the following form:
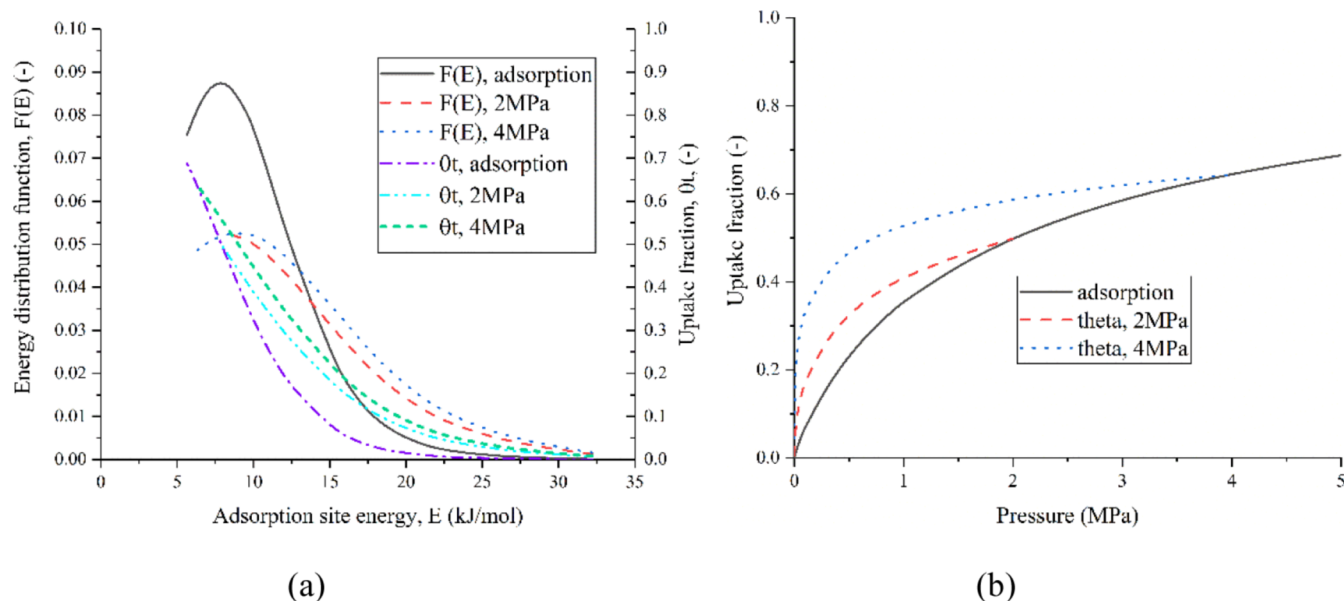
Figure 9. (a) Site energy distribution function, $F(E)$, and cumulative uptake, $\theta_t(E)$, according to the adsorption and desorption isotherms for different initial pressures (2 and 4 MPa) and (b) corresponding desorption isotherm (given that $T = 295$ K, $p_M = 2, 4$ MPa, $K_{LF} = 0.5$ MPa^{-1}, $n = 0.86$, and HI = 0.4).
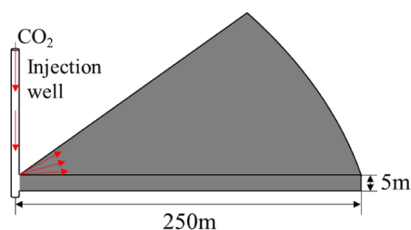

Figure 10. Schematic of the radially symmetric CO_2 injection geometry.

$$C_s = \frac{[C_L(K_{LF}p_M^{HI})^{1/(1-HI)}p]^{n(1-HI)}}{1 + [C_L(K_{LF}p_M^{HI})^{1/(1-HI)}p]^{n(1-HI)}} \tag{23}$$

Because the HI ranges from 0 to 1, $n(1 - HI) < n$ if sorption is not fully reversible. Assuming that the site energy distribution can be captured by the quasi-Gaussian distribution following adsorption, the reduction of the isotherm constant n indicates the increase in energetic heterogeneity.

Meanwhile, mean site energy is also altered, and changes in mean site energy depend on the pressure for desorption initialization and the degree of sorption hysteresis. Figure 8 shows a comparison of site energy distributions for adsorption and desorption isotherms (Figure 8a). Different degrees of sorption hysteresis are considered, as shown in Figure 8b. It can be observed that after the gas–solid interaction, the frequency of sites with lower and higher binding energy increases, while sites with mediating energy decrease significantly. This suggests that the pores with smaller size and larger size will increase after adsorption. The predicted pore structure change is similar to experimental measurements of Wang et al.[49] and Geng et al.[50] Variation of the pore structure can be attributed to adsorption-induced pore deformation and structural rearrangement.[51] Since there is a negative correlation between pore size and adsorption energy,[39] adsorption sites with higher binding energy is increased, and more activation energy from a larger gas pressure drop is required for desorption. This is why sorption hysteresis

occurs. Another notable feature is the influence on mean energy. The mean energy increases from 7.9 to 9.0 and 10.4 kJ/mol for HI = 0.4 and 0.6, respectively. Due to the lower contribution of lower energy sites, the adsorption capacity drops after re-adsorption.

5.3. Effect of Initialized Pressure for Desorption. The dependence of desorption characteristics on the initial pressure at which depressurization begins has been observed in previous sections. Figure 9 shows the effect of pressures for adsorption on the site energy distribution. It is observed that when the maximum pressure during adsorption is higher, or the initial pressure where desorption begins is higher, a larger fraction of sites with intermediate binding energy will transform into high binding energy sites, as indicated by changes in the frequency of site energy shown in Figure 9a. As a result, under higher pressure condition, even a larger pressure drop could only release less adsorbed gas molecules when the initialized pressure for desorption is higher, as shown in Figure 9b. In practice, reducing pressure to zero is difficult, and there will be residual adsorbed gas in sorbents such as coal and shale reservoirs.

5.4. Influence of Sorption Hysteresis on the Long-Term Fate of CO_2 Sequestration. Gas sorption hysteresis can influence CBM recovery, shale gas recovery, and CO_2 sequestration in coalbeds. It is beneficial to CO_2 sequestration as coal surfaces can retain substantial amounts of injected CO_2 even though the gas pressure reduces. In this subsection, the influence of sorption hysteresis on the long-term fate of injected CO_2 will be investigated via numerical simulation. The numerical model and model inputs are presented in Appendix B. The axisymmetric simulation domain is considered, as illustrated in Figure 10, with the axis of symmetry along the axis of the injection well. The radius of the coal seam is chosen to be 250 m from the injection well. For 1 year, CO_2 is continuously injected through the vertical wellbore at a constant injection pressure of 6 MPa. Then, the injection is stopped. The simulation runs for 20 years. The effects of different degrees of sorption hysteresis in the post-injection period are considered
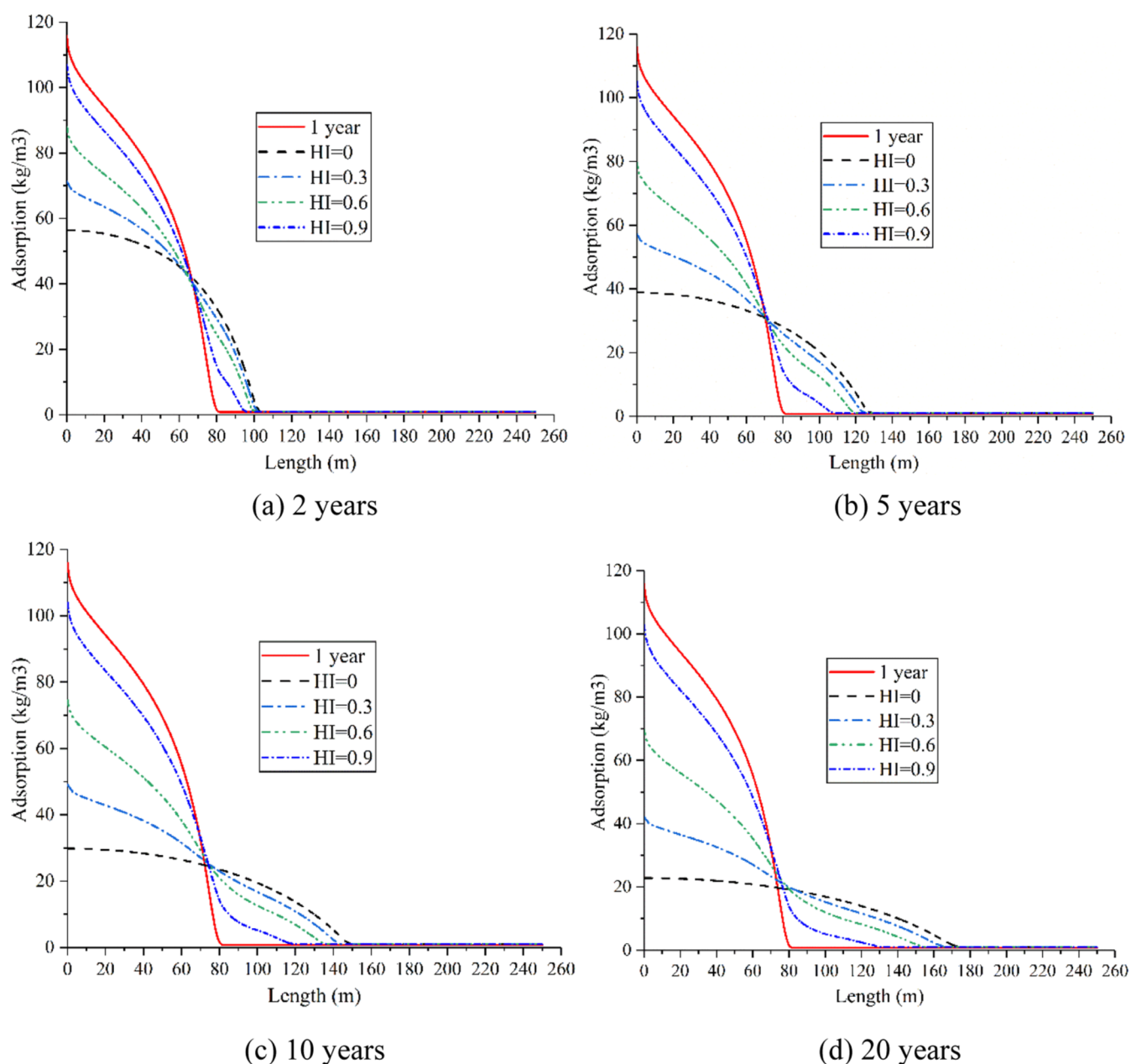
Figure 11. Profiles of adsorbed CO_2 along the radial distance for different degrees of sorption hysteresis: (a) 2, (b) 5, (c) 10, and (d) 20 years.

through defining different hysteresis indices HI = 0.0, 0.3, 0.6, and 0.9.

Figure 11 shows the amount of adsorbed CO_2 distribution along the radius after 2, 5, 10, and 20 years. The red line in Figure 11 is the adsorbed CO_2 distribution after the injection is stopped (1 year). It can be observed that the CO_2 front continues to advance outward in a radially symmetric pattern after the injection is stopped, while this advancement is much slower. After 1 year of injection, the CO_2 front reaches about 80 m away from the injection well, and it reaches approximately 175 m after 20 years when sorption is fully reversible. When CO_2 adsorption hysteresis is significant ($H = 0.9$), the CO_2 front only arrives at 130 m after 20 years. This can be attributed to the following: (1) the gas spreading area increases with the increase in distance from the injection well and (2) the gas pressure as a driving force for free phase flow becomes lower as time increases, as shown in Figure 12.

In addition, the adsorbed CO_2 in the area close to the injection will decrease as a result of desorption as time increases. The weaker the degree of adsorption hysteresis is, the greater the drop of adsorbed CO_2 is. For example, the adsorbed CO_2 in the vicinity of the well drops from 116 to 30, 49, 74, and 104 kg/m^3 after 10 years for HI = 0, 0.3, 0.6, and 0.9, respectively, as shown in Figure 11c. From Figure 12, it can be seen that once the injection event is suspended, the pressure in the region close to the well drops immediately. After 2 years, the pressure drops to less than 1 MPa for all degrees of adsorption hysteresis. In contrast to the adsorbed amount, CO_2 pressure undergoes a larger decrease when the degree of adsorption hysteresis is significant. This is because when adsorption hysteresis is stronger, more adsorption sites with higher binding energy exist, and the desorption of adsorbed CO_2 requires a larger pressure drop, as shown in Figure 8b. Less adsorbed CO_2 can desorb as a supplement to free phase CO_2. On the other hand,
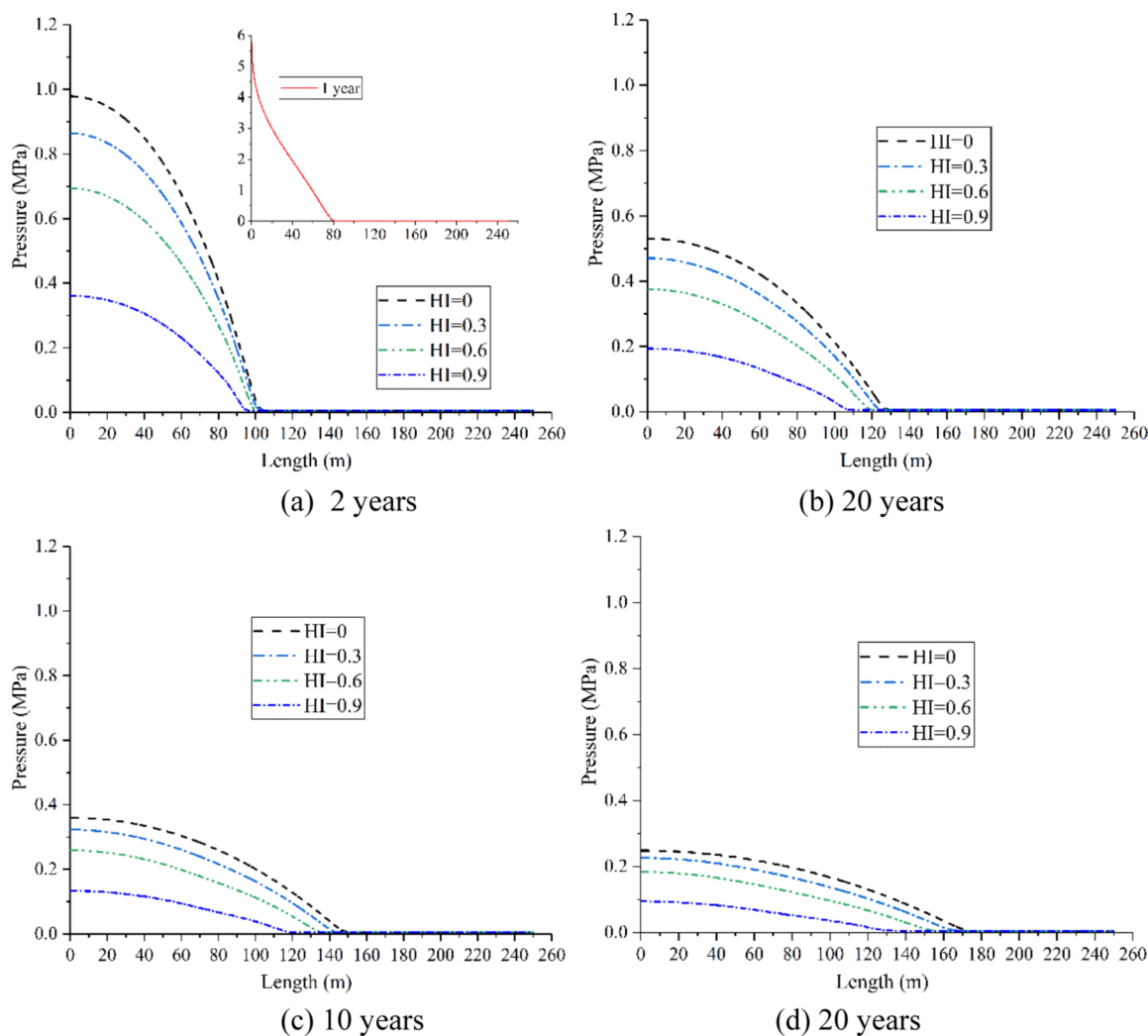
Figure 12. Profiles of CO_2 pressure along the radial distance for different degrees of sorption hysteresis: (a) 2, (b) 5, (c) 10, and (d) 20 years.

the free gas can continue to propagate further into the region far from the injection well, which also causes a decrease in the free phase CO_2 concentration. These leads to a more significant drop in pressure, while the adsorbed CO_2 concentration remains higher. It can be concluded that due to a considerable drop in pressure after years, the propagation of injected CO_2 will be slower, and it may even stop when adsorption hysteresis of CO_2 in coal is significant. This implies that the coal seam that shows significant adsorption hysteresis is beneficial for long-term storage of CO_2.

The proposed model includes both adsorption and desorption isotherms, and it provides an effective tool to accurately estimate the production of CBM, shale gas recovery, CO_2 leakage, or plume migration. When ignoring desorption, its contribution to gas production is overestimated. The aforementioned analyses suggest that when sorption hysteresis is stronger, depressurization must reach to a minimum value to release adsorbed methane. The model is able to provide quantitative estimation of depressurization, which is significant for better assessment of gas exploitation and management.

6. CONCLUSIONS

This work develops an adsorption−desorption model for representing the adsorption isotherm and desorption isotherm of gases with hysteresis. The developed model captures the

energetically heterogeneous surface of an adsorbent with the concept of patchwise topography and the ASED. To characterize the sorption hysteresis behavior, the HI as a measure of the degree of sorption hysteresis is derived based on the difference in site energy distribution for adsorption and desorption isotherms. In particular, the impact of initialized pressure where desorption begins on the desorption process is accounted for in the proposed model. To examine the ability of the proposed model to capture the adsorption and desorption behavior, a set of validation tests were conducted against experimental data on adsorption/desorption of various gases in coal and shale, and good agreements were achieved. The sensitivity analysis on the model parameters indicates that the gas−coal interaction alters the site energy distribution, and the initialized pressure where desorption begins and the degree of sorption hysteresis are able to influence the variation of the site energy distribution. It is revealed that the adsorption-induced change in pore size distribution is the underlying mechanism for desorption hysteresis occurrence. This work provides an effective tool to predict the adsorption and desorption isotherms of gases in coal and shales. It can be used for accurate estimation of gas production or shale gas exploration and production and evaluating the long-term fate of CO_2 storage.

◼ APPENDIX A

Table A1 lists the parameters used for matching experimental data from Zhao et al.[31] Figures A1 and A2 present the

Table A1. Model Parameters for Fitting the Data of Zhao et al.[31] on Shale Samples[a]

samples	adsorption capacity (mol/kg)	constant, K_{LF}, (bar^{-1})	exponent, n, ($-$)	exponent, HI, ($-$)
K-CO$_2$	2.34	0.011	0.709	0.168
K-CH$_4$	0.51	0.022	0.869	0.179
K-C$_2$H$_6$	7.98	4.79×10^{-4}	0.584	0.483
K-C$_3$H$_8$	37.72	1.11×10^{-4}	0.603	0.450
K-n-C$_4$H$_{10}$	35.93	1.01×10^{-3}	0.703	0.581
K-iso-C$_4$H$_{10}$	18.63	4.15×10^{-4}	0.616	0.610
N-CO$_2$	3.42	1.18×10^{-4}	0.626	0.128
N-CH$_4$	0.12	8.97×10^{-3}	0.821	0.196
N-C$_2$H$_6$	5.51	9.33×10^{-5}	0.669	0.142
N-C$_3$H$_8$	12.81	1.67×10^{-4}	0.728	0.210
N-n-C$_4$H$_{10}$	15.42	5.93×10^{-4}	0.762	0.272
N-iso-C$_4$H$_{10}$	2.02	2.19×10^{-3}	0.692	0.203

comparison of results between the model and experimental measurements.

◼ APPENDIX B

B1. Theory

Considering the two distinct porosity systems of coal reservoirs, the dual porosity model is usually used to represent the flow process of fluid in coals, for example.[45,52,53] The governing equations for fluid flow in dual porosity media are written as

$$\frac{\partial(\rho_f \, \phi_f)}{\partial t} = -\nabla \cdot (\mathbf{v}\rho_f) - \Gamma_{mf} \tag{B1}$$

$$\frac{\partial(\rho_m \, \phi_m)}{dt} = Q_s + \Gamma_{mf} \tag{B2}$$

where ρ_f and ρ_m are the gas densities in the fracture and matrix, respectively, ϕ_f and ϕ_m are the porosities of both continua, $\mathbf{v}$ is the flow velocity, Γ_{mf} is the mass transfer between fracture and matrix continua, and Q_s is the gas source. The source term Q_s in this work is only considered from gas adsorption, and eqs 12 and 18 are applied for calculation of the source term during adsorption and desorption, respectively.
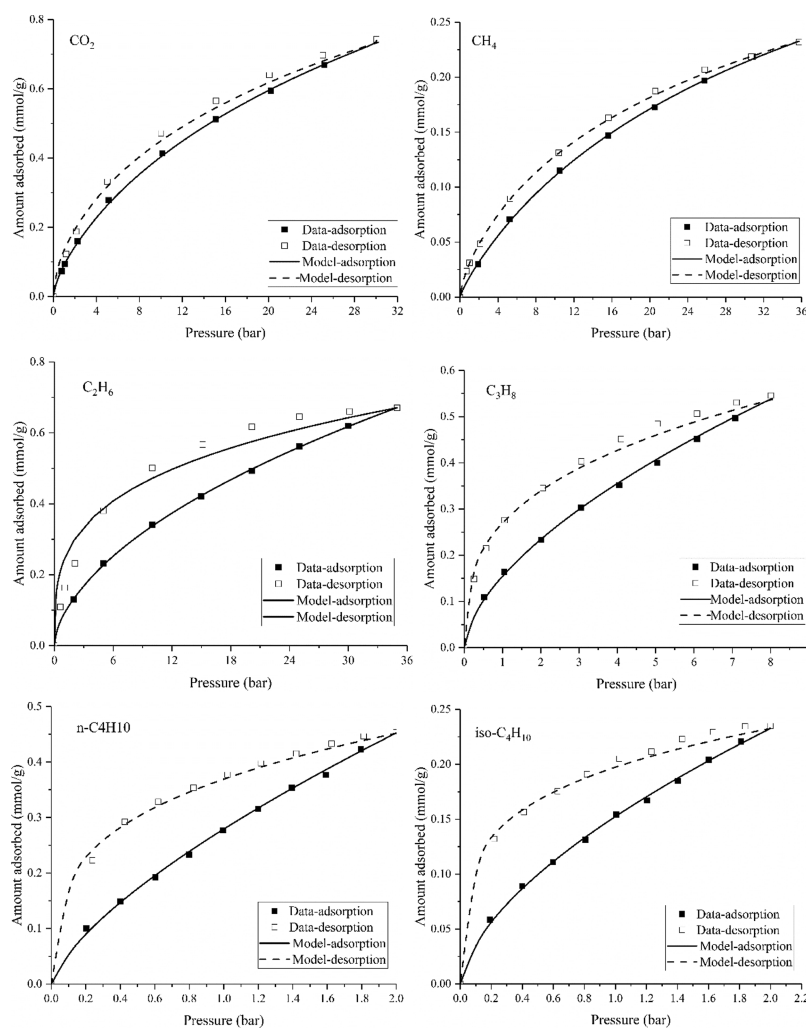

Figure A1. Results of the model fitting the experimental data by Zhao, Lai, and Firoozabadi[31] on adsorption/desorption of various hydrocarbons and CO$_2$ in Kimmeridge Blackstone.
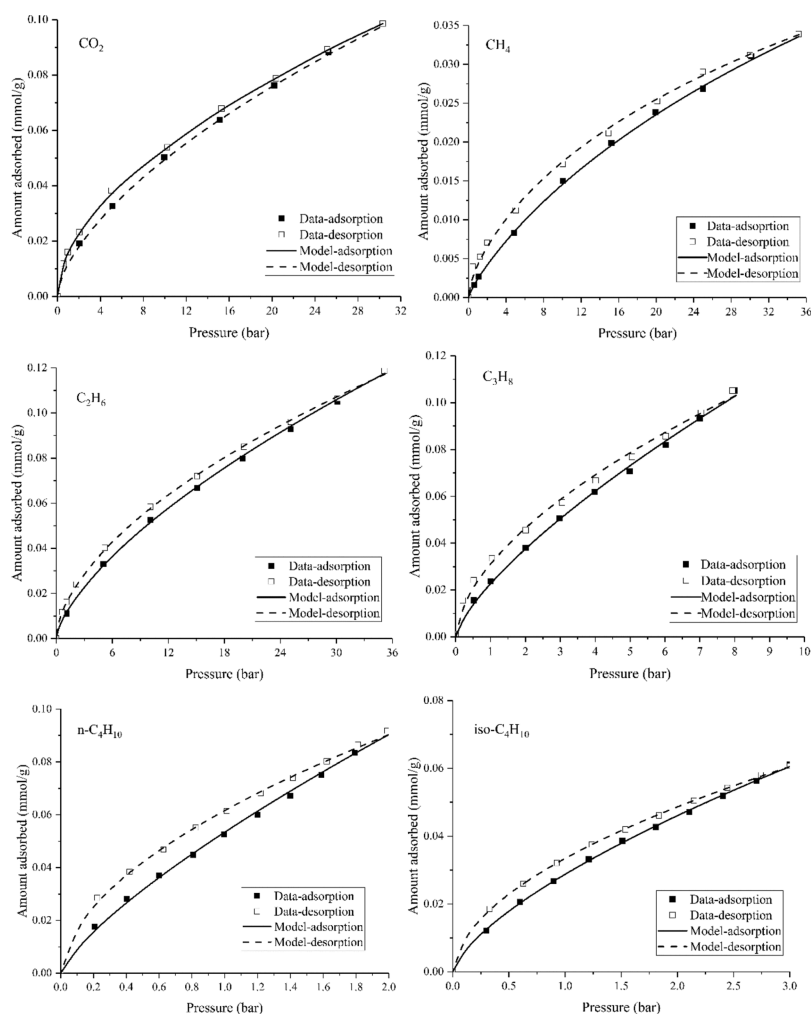
Figure A2. Results of the model fitting the experimental data by Zhao, Lai, and Firoozabadi[31] on adsorption/desorption of various hydrocarbons and CO_2 in Neuquén Shale.

The fluid flow velocity is described by the Darcy's law

$$v = -\frac{k}{\mu}\nabla p_f \tag{B3}$$

where k is the fracture permeability, the stress-dependent permeability model by Chen, et al.[54] is used for estimating permeability evolution, μ is the viscosity of the gas, p_f is the gas pressure, which can be estimated using the real gas law $p_f = ZRT\rho_f/M$, Z is the gas compressibility factor, which is calculated using the Peng−Robinson equation of state, R is the universal gas constant, T is the temperature, and M is the molar mass.

The mass transfer term in eqs B1 and B2 depends on the mass exchange rate and the difference between the gas concentrations in the fracture continuum and matrix continuum,[45,55] given as

$$\Gamma_{mf} = \frac{1}{\tau}(\rho_f - \rho_m) \tag{B4}$$

where τ is the diffusion time.

B2. Model Input

Table B1 shows the input parameters for the numerical simulation.

Table B1. Input Parameters for the Numerical Simulation

material parameters	values
porosity of the coal matrix, ϕ_m (−)	0.045
porosity of the fracture, ϕ_f (−)	0.018
initial permeability, k (m²)	3.6×10^{-15}
gas viscosity, μ (Pa·s)	1.84×10^{-5}
density of coal, ρ_c (kg/m³)	1470
diffusion time, τ (s)	2.0×10^5
maximum adsorption amount, C_L (mol/kg)	2.49
constant of the LF isotherm, K_{LF} (MPa⁻¹)	0.496
exponent of the LF isotherm, n, (−)	0.861
sorption HI, H (−)	0.3, 0.6, and 0.9
temperature, T, (K)	303

■ AUTHOR INFORMATION

Corresponding Author

    Min Chen − *Geoenvironmental Research Centre, School of Engineering, Cardiff University, Cardiff CF24 3AA, U.K.;* ⓘ orcid.org/0000-0003-0809-7436; Email: chenm24@ Cardiff.ac.uk

Authors

    Shakil A. Masum − *Geoenvironmental Research Centre, School of Engineering, Cardiff University, Cardiff CF24 3AA, U.K.*

Sivachidambaram Sadasivam − *Geoenvironmental Research Centre, School of Engineering, Cardiff University, Cardiff CF24 3AA, U.K.;* ⊙ orcid.org/0000-0002-2305-0292

Hywel R. Thomas − *Geoenvironmental Research Centre, School of Engineering, Cardiff University, Cardiff CF24 3AA, U.K.*

Andrew C. Mitchell − *Department of Geography and Earth Sciences, Aberystwyth University, Aberystwyth SY23 3DB, U.K.*

Complete contact information is available at:
https://pubs.acs.org/10.1021/acs.energyfuels.2c03441

Notes
The authors declare no competing financial interest.

■ REFERENCES

(1) Weniger, P.; Kalkreuth, W.; Busch, A.; Krooss, B. M. High-pressure methane and carbon dioxide sorption on coal and shale samples from the Paraná Basin, Brazil. *Int. J. Coal Geol.* **2010**, *84*, 190−205.

(2) Wang, K.; Li, H.; Wang, J.; Jiang, B.; Bu, C.; Zhang, Q.; Luo, W. Predicting production and estimated ultimate recoveries for shale gas wells: A new methodology approach. *Appl. Energy* **2017**, *206*, 1416−1431.

(3) Chen, M.; Masum, S.; Thomas, H. Modeling adsorption and transport behavior of gases in moist coal matrix. *Energy Fuels* **2021**, *35*, 13200−13214.

(4) Zhang, X. G.; Ranjith, P. G.; Perera, M. S. A.; Ranathunga, A. S.; Haque, A. Gas Transportation and Enhanced Coalbed Methane Recovery Processes in Deep Coal Seams: A Review. *Energy Fuels* **2016**, *30*, 8832−8849.

(5) Memon, A.; Li, A.; Memon, B. S.; Muther, T.; Han, W.; Kashif, M.; Tahir, M. U.; Akbar, I. Gas adsorption and controlling factors of shale: review, application, comparison and challenges. *Nat. Resour. Res.* **2021**, *30*, 827−848.

(6) Bhowmik, S.; Dutta, P. A study on the effect of gas shale composition and pore structure on methane sorption. *J. Nat. Gas Sci. Eng.* **2019**, *62*, 144−156.

(7) Kim, H. J.; Shi, Y.; He, J.; Lee, H.-H.; Lee, C.-H. Adsorption characteristics of CO₂ and CH₄ on dry and wet coal from subcritical to supercritical conditions. *Chem. Eng. J.* **2011**, *171*, 45−53.

(8) Chen, M.; Masum, S.; Thomas, H. Modeling Non-isothermal Transport Behavior of Real Gas in Deformable Coal Matrix. *Energy Fuels* **2020**, *35*, 1605−1619.

(9) Wang, K.; Wang, G.; Ren, T.; Cheng, Y. Methane and CO₂ sorption hysteresis on coal: A critical review. *Int. J. Coal Geol.* **2014**, *132*, 60−80.

(10) Hou, X.; Liu, S.; Zhu, Y.; Yang, Y. Experimental and theoretical investigation on sorption kinetics and hysteresis of nitrogen, methane, and carbon dioxide in coals. *Fuel* **2020**, *268*, 117349.

(11) Ekundayo, J. M.; Rezaee, R.; Fan, C. Experimental investigation and mathematical modelling of shale gas adsorption and desorption hysteresis. *J. Nat. Gas Sci. Eng.* **2021**, *88*, 103761.

(12) Cai, X.; Li, D.; Zhang, D. Methane Adsorption and Desorption on a Deep Shale Matrix under Simulative Reservoir Temperature and Pressure. *Energy Fuels* **2022**, *36*, 11888−11902.

(13) Sadasivam, S.; Masum, S.; Chen, M.; Stańczyk, K.; Thomas, H. Kinetics of gas phase CO₂ adsorption on bituminous coal from a shallow coal seam. *Energy Fuels* **2022**, *36*, 8360−8370.

(14) Bell, G. J.; Rakop, K. C. *Hysteresis of Methane/coal Sorption Isotherms*; SPE Annual Technical Conference and Exhibition; OnePetro, 1986.

(15) Ekundayo, J. M.; Rezaee, R. Numerical simulation of gas production from gas shale reservoirs—influence of gas sorption hysteresis. *Energies* **2019**, *12*, 3405.

(16) Pinson, M. B.; Masoero, E.; Bonnaud, P. A.; Manzano, H.; Ji, Q.; Yip, S.; Thomas, J. J.; Bazant, M. Z.; Van Vliet, K. J.; Jennings, H. M. Hysteresis from multiscale porosity: modeling water sorption and shrinkage in cement paste. *Phys. Rev. Appl.* **2015**, *3*, 064009.

(17) Cui, L. Y.; Ye, W. M.; Wang, Q.; Chen, Y. G.; Chen, B.; Cui, Y. J. Insights into determination of gas breakthrough in saturated compacted gaomiaozi bentonite. *J. Mater. Civ. Eng.* **2020**, *32*, 04020190.

(18) Mason, G. A model of adsorption-desorption hysteresis in which hysteresis is primarily developed by the interconnections in a network of pores. *Proc. R. Soc. London, A* **1983**, *390*, 47−72.

(19) Chen, J.; Wang, F.; Liu, H.; Wu, H. Molecular mechanism of adsorption/desorption hysteresis: dynamics of shale gas in nanopores. *Sci. China Phys. Mech. Astron.* **2017**, *60*, 1−8.

(20) Grosman, A.; Ortega, C. Capillary condensation in porous materials. Hysteresis and interaction mechanism without pore blocking/percolation process. *Langmuir* **2008**, *24*, 3977−3986.

(21) Nie, B.; Liu, X.; Yang, L.; Meng, J.; Li, X. Pore structure characterization of different rank coals using gas adsorption and scanning electron microscopy. *Fuel* **2015**, *158*, 908−917.

(22) Yang, R.; He, S.; Yi, J.; Hu, Q. Nano-scale pore structure and fractal dimension of organic-rich Wufeng-Longmaxi shale from Jiaoshiba area, Sichuan Basin: Investigations using FE-SEM, gas adsorption and helium pycnometry. *Mar. Petrol. Geol.* **2016**, *70*, 27−45.

(23) Alafnan, S. *Adsorption−Desorption Hysteresis in Shale Formation: New Insights into the Underlying Mechanisms*; Energy & Fuels, 2022.

(24) Ozdemir, E.; Morsi, B. I.; Schroeder, K. Importance of volume effects to adsorption isotherms of carbon dioxide on coals. *Langmuir* **2003**, *19*, 9764−9773.

(25) Chen, Y.; Qin, Y.; Li, Z.; Shi, Q.; Wei, C.; Wu, C.; Cao, C.; Qu, Z. Differences in desorption rate and composition of desorbed gases between undeformed and mylonitic coals in the Zhina Coalfield, Southwest China. *Fuel* **2019**, *239*, 905−916.

(26) Goodman, A.; Busch, A.; Duffy, G.; Fitzgerald, J.; Gasem, K.; Gensterblum, Y.; Krooss, B. M.; Levy, J.; Ozdemir, E.; Pan, Z.; Robinson, R. L.; Schroeder, K.; Sudibandriyo, M.; White, C. M. An inter-laboratory comparison of CO₂ isotherms measured on Argonne premium coal samples. *Energy Fuels* **2004**, *18*, 1175−1182.

(27) Sander, M.; Lu, Y.; Pignatello, J. J. A thermodynamically based method to quantify true sorption hysteresis. *J. Environ. Qual.* **2005**, *34*, 1063−1072.

(28) Zhu, H.; Selim, H. Hysteretic behavior of metolachlor adsorption-desorption in soils. *Soil Sci.* **2000**, *165*, 632−645.

(29) Busch, A.; Gensterblum, Y.; Krooss, B. M.; Littke, R. Methane and carbon dioxide adsorption−diffusion experiments on coal: upscaling and modeling. *Int. J. Coal Geol.* **2004**, *60*, 151−168.

(30) Zhou, Y.; Zhang, R.; Wang, J.; Huang, J.; Li, X.; Wu, J. Desorption hysteresis of CO₂ and CH₄ in different coals with cyclic desorption experiments. *J. CO₂ Util.* **2020**, *40*, 101200.

(31) Zhao, H.; Lai, Z.; Firoozabadi, A. Sorption hysteresis of light hydrocarbons and carbon dioxide in shale and kerogen. *Sci. Rep.* **2017**, *7*, 1−10.

(32) Kamiya, Y.; Mizoguchi, K.; Terada, K.; Fujiwara, Y.; Wang, J.-S. CO2 sorption and dilation of poly (methyl methacrylate). *Macromolecules* **1998**, *31*, 472−478.

(33) Chen, M.; Coasne, B.; Guyer, R.; Derome, D.; Carmeliet, J. Role of hydrogen bonding in hysteresis observed in sorption-induced swelling of soft nanoporous polymers. *Nat. Commun.* **2018**, *9*, 3507.

(34) McCutcheon, A.; Barton, W.; Wilson, M. Kinetics of water adsorption/desorption on bituminous coals. *Energy Fuel.* **2001**, *15*, 1387−1395.

(35) Kumar, K. V.; Gadipelli, S.; Wood, B.; Ramisetty, K. A.; Stewart, A. A.; Howard, C. A.; Brett, D. J.; Rodriguez-Reinoso, F. Character-

ization of the adsorption site energies and heterogeneous surfaces of porous materials. *J. Mater. Chem. A* **2019**, *7*, 10104−10137.

(36) Rudziński, W.; Borowiecki, T.; Dominko, A.; Pańczyk, T. A new quantitative interpretation of temperature-programmed desorption spectra from heterogeneous solid surfaces, based on statistical rate theory of interfacial transport: the effects of simultaneous readsorption. *Langmuir* **1999**, *15*, 6386−6394.

(37) Rudzinski, W.; Panczyk, T. The Langmuirian adsorption kinetics revised: a farewell to the XXth century theories? *Adsorption* **2002**, *8*, 23−34.

(38) Dobruskin, V. K. Physical adsorption in micropores: a condensation approximation approach. *Langmuir* **1998**, *14*, 3847−3857.

(39) Burhan, M.; Shahzad, M. W.; Ng, K. C. A universal theoretical framework in material characterization for tailored porous surface design. *Sci. Rep.* **2019**, *9*, 8773.

(40) Panczyk, T.; Rudzinski, W. A simultaneous description of kinetics and equilibria of adsorption on heterogeneous solid surfaces based on the statistical rate theory of interfacial transport. *Langmuir* **2003**, *19*, 1173−1181.

(41) Panczyk, T.; Rudzinski, W. Kinetics of multisite-occupancy adsorption on heterogeneous solid surfaces: a statistical rate theory approach. *J. Phys. Chem. B* **2002**, *106*, 7846−7851.

(42) Ng, K. C.; Burhan, M.; Shahzad, M. W.; Ismail, A. B. A universal isotherm model to capture adsorption uptake and energy distribution of porous heterogeneous surface. *Sci. Rep.* **2017**, *7*, 10634.

(43) Jessen, K.; Tang, G.-Q.; Kovscek, A. R. Laboratory and simulation investigation of enhanced coalbed methane recovery by gas injection. *Transp. Porous Media* **2008**, *73*, 141−159.

(44) He, X.; Cheng, Y.; Hu, B.; Wang, Z.; Wang, C.; Yi, M.; Wang, L. Effects of coal pore structure on methane-coal sorption hysteresis: an experimental investigation based on fractal analysis and hysteresis evaluation. *Fuel* **2020**, *269*, 117438.

(45) Chen, M.; Hosking, L. J.; Sandford, R. J.; Thomas, H. R. Dual porosity modelling of the coupled mechanical response of coal to gas flow and adsorption. *Int. J. Coal Geol.* **2019**, *205*, 115−125.

(46) Borisover, M. Accumulated Gibbs free energy as a quantitative measure of desorption hysteresis associated with the formation of metastable states. *Chemosphere* **2019**, *215*, 490−499.

(47) Stoeckli, H.; Kraehenbuehl, F.; Ballerini, L.; De Bernardini, S. Recent developments in the Dubinin equation. *Carbon* **1989**, *27*, 125−128.

(48) Li, J.; Wu, K.; Chen, Z.; Wang, W.; Yang, B.; Wang, K.; Luo, J.; Yu, R. Effects of energetic heterogeneity on gas adsorption and gas storage in geologic shale systems. *Appl. Energy* **2019**, *251*, 113368.

(49) Wang, Z.; Cheng, Y.; Zhang, K.; Hao, C.; Wang, L.; Li, W.; Hu, B. Characteristics of microscopic pore structure and fractal dimension of bituminous coal by cyclic gas adsorption/desorption: An experimental study. *Fuel* **2018**, *232*, 495−505.

(50) Geng, W.; Huang, G.; Guo, S.; Jiang, C.; Dong, Z.; Wang, W. Influence of long-term CH_4 and CO_2 treatment on the pore structure and mechanical strength characteristics of Baijiao coal. *Energy* **2022**, *242*, 122986.

(51) Larsen, J. W. The effects of dissolved CO_2 on coal structure and properties. *Int. J. Coal Geol.* **2004**, *57*, 63−70.

(52) Hosking, L. J.; Chen, M.; Thomas, H. R. Numerical analysis of dual porosity coupled thermo-hydro-mechanical behaviour during CO_2 sequestration in coal. *Int. J. Rock Mech. Min. Sci.* **2020**, *135*, 104473.

(53) Masum, S. A.; Chen, M.; Hosking, L. J.; Stańczyk, K.; Kapusta, K.; Thomas, H. R. A numerical modelling study to support design of an in-situ CO_2 injection test facility using horizontal injection well in a shallow-depth coal seam. *Int. J. Greenh. Gas Control* **2022**, *119*, 103725.

(54) Chen, M.; Masum, S.; Sadasivam, S.; Thomas, H. Modelling anisotropic adsorption-induced coal swelling and stress-dependent anisotropic permeability. *Int. J. Rock Mech. Min. Sci.* **2022**, *153*, 105107.

(55) Chen, M.; Masum, S.; Thomas, H. 3D hybrid coupled dual continuum and discrete fracture model for simulation of CO_2 injection into stimulated coal reservoirs with parallel implementation. *Int. J. Coal Geol.* **2022**, *262*, 104103.